

Estimation of Full Sky CMB Angular Power Spectrum from High Resolution Partial Sky CMB Map Using Artificial Neural Network

Srikanta Pal^{1*}, Pallav Chanda^{1†} and Rajib Saha^{1‡}

¹Department of Physics, Indian Institute of Science Education and Research, Bhopal-462066, India

Abstract

Reliable extraction of cosmological information from observed *cosmic microwave background* (CMB) maps requires accurate removal of foreground components. Since some regions of the sky are inevitably contaminated by strong foreground signals, it may be desired to excise such strongly contaminated regions even after a foreground subtraction has been performed. In this article, we employ an *artificial neural network* (ANN) to predict the full sky CMB angular power spectrum from the partial sky spectrum obtained from masked CMB temperature anisotropy map, at a high pixel resolution. We use a simple ANN architecture with one hidden layer containing 895 neurons. Using 1.2×10^5 training samples of full sky and corresponding partial sky CMB angular power spectra at Healpix pixel resolution parameter $N_{side} = 256$, we show that predicted spectrum by our ANN agrees well with the *target* spectrum at each realization for the multipole range $2 \leq l \leq 512$. The predicted spectra are statistically unbiased and they preserve the cosmic variance accurately. Statistically, the differences between the mean predicted and underlying theoretical spectra are within 3σ . Moreover, the probability densities obtained from predicted angular power spectra agree very well with those obtained from 'actual' full sky CMB angular power spectra for each multipole. Equally interesting is that the correlation matrix calculated from predicted angular power spectra does not show any signature of correlation between the angular power spectrum of different multipoles. Our work shows that the predicted spectra do not need to

*email:srikanta18@iiserb.ac.in , psrikanta357@gmail.com

†email:pallavchanda24@gmail.com

‡email:rajib@iiserb.ac.in

be binned even at high resolution to rid of correlations due to *mode-mode coupling* introduced on the partial sky since the ANN learns to effectively recover the lost information due to sky cut. The excellent agreement of statistical properties between the predicted and the ground-truth demonstrates the importance of using artificial intelligence systems in cosmological analysis more widely.

Keywords: Cosmology; *Cosmic microwave background* (CMB); Data analysis; *Artificial neural network* (ANN)

1 Introduction

Cosmic microwave background (CMB) radiation, first detected by [Penzias & Wilson \(1965\)](#), originated from the so-called surface of last scattering with a temperature $\approx 2970K$ and fills the space with a blackbody temperature of $2.72K$ today ([Fixsen et al., 1996](#); [Mather et al., 1999](#)). This radiation contains tiny anisotropies and inhomogeneities which encode the fundamental information about the initial conditions on the metric fluctuations (induced by the quantum fluctuations of inflaton ([Guth & Pi, 1982](#)) field) as well as the detailed history of physical interaction of the CMB photons with gravitation and other entities during the later development of the Universe. Accurate measurements and unambiguous usage of this *gift of the nature* is therefore of absolute importance for understanding our universe reliably. Satellite-based experiments, like Planck ([Planck Collaboration VI, 2020](#)), WMAP ([Hinshaw et al., 2013](#)), COBE ([Bennett et al., 1996](#)), and ground-based experiments, such as SPT ([Hou et al., 2014](#)), ACT ([Sievers et al., 2013](#)) constrained cosmological parameters using CMB observations. Some future experiments of CMB, Echo (aka CMB-Bharat¹), CCAT-prime ([Stacey et al., 2018](#)), PICO ([Hanany et al., 2019](#)), LiteBird ([Hazumi et al., 2020](#)) have also been proposed to meet the monumental promise the CMB provides to understand physics of the very early Universe.

Under the assumptions of Gaussianity ([Guth & Pi, 1982](#); [Allen et al., 1987](#); [Falk et al., 1992](#); [Gangui et al., 1994](#); [Acquaviva et al., 2003](#); [Maldacena, 2003](#)) and statistical isotropy ([Hajian & Souradeep, 2004](#)) of the CMB, all statistical information of the later is encoded in the two-point correlation functions which can be represented by the angular power spectrum in the harmonic space. Estimation of this spectrum is a challenging task from the observed CMB map since astrophysical emissions from the local Universes (e.g., several diffused emissions from Milky Way and localized emissions from extragalactic point sources) contaminate

¹<http://cmb-bharat.in/>

the primordial and weak CMB signal. Some regions of the sky may be so heavily contaminated by the local foregrounds that even after a foreground subtraction has been performed such regions must be removed entirely from the cosmological analysis since any residual foregrounds creeping in from these regions may potentially bias the cosmological interpretation. Consequently, the angular power spectrum estimated from the resulting incomplete sky loses its well-behaved statistical properties that are otherwise present in its full sky descriptions. Due to the loss of orthogonality conditions of the spherical harmonics on the partial sky, the CMB modes on all angular scales become correlated and biased low. Since cosmological theory predicts only the full sky CMB angular power spectrum, it is important to estimate the actual full sky spectrum even after any sky-mask has been applied.

In this article, we use an *artificial neural network* (ANN) to achieve this purpose using high pixel resolution CMB maps for the multipole range $2 \leq l \leq 512$. An earlier work (Chanda & Saha, 2021) in this direction discussed this problem over only large angular scales on the sky ($2 \leq l \leq 32$). An important advantage of our method is that we are able to predict the ground-truth full sky spectra at each multipole without any need to estimate the band average spectrum which we otherwise do to reduce the correlation due to *mode-mode coupling* over the partial sky and to account for the lost information in presence of sky cuts. Since our ANN effectively learns to get back the lost information due to masking, it can reproduce the 'actual' full sky spectrum at each angular scale l (within small random fluctuations) but without introducing any correlations between the spectrum of different multipoles even at any given sky realization. We demonstrate that our multipole-wise recovered spectra are statistically completely equivalent to the underlying full sky spectra by computing the correlations matrix and cosmic variance of the former. The realization specific accurate reconstruction of the ground-truth over a wide angular scale is encouraging and demands further utilization of the ANN in the analysis of CMB angular power spectrum.

In the current work, we evolve the procedure of Chanda & Saha (2021) with some modifications. Chanda & Saha (2021) used an ANN with two hidden layers each containing 1024 neurons to predict the full sky spectrum from the partial sky $N_{side} = 16$ CMB maps. In their work, they used a *concrete dropout* method (Gal et al., 2017), for reducing epistemic uncertainties of the ANN model. Our ANN consists of only one hidden layer with 895 neurons and we utilize $N_{side} = 256$ partial sky CMB maps. We employ *model averaging ensemble* method (Lai et al., 2021) in place of *concrete dropout* for minimizing epistemic uncertainties of our ANN model. When applied on the Planck data (Planck Collaboration IV, 2020), our ANN gives excellent agreements between the predicted and inpainted full sky spectra for COMMANDER, NILC, SMICA, SEVEM foreground cleaned CMB

maps².

In the contemporary literature, machine learning (ML) found its applications in several fields of physics, e.g. *high energy physics, particle physics, cosmology, observational astrophysics* (Olvera, Gómez-Vargas & Vázquez, 2021). An advantage of ML is that although the Metropolis-Hastings algorithm for Bayesian inference in cosmology may be computationally expensive for large volumes of data, ANN permits a decrease in the computational time (Graff et al., 2012; Moss, 2020; Hortua et al., 2020; Gómez-Vargas, Esquivel et al., 2021). Various types of ANN were implemented by Mancini et al. (2022) for the purpose of parameter estimations using CMB data, which showed that the Bayesian process can speed using ANNs. In the literature (Escamilla-Rivera et al., 2020; Wang et al., 2020; Dialektopoulos et al., 2021; Gómez-Vargas, Vázquez et al., 2021), we also see the operation of ANNs for non-parametric reconstructions of cosmological functions. Baccigalupi et al. (2000) separated different types of foreground signal, such as thermal dust emissions, galactic synchrotron and radiation emitted by galaxy clusters from CMB maps using ANN. Petroff et al. (2020) implemented a neural network to classify the noises from the anisotropies of CMB temperatures.

On the more traditional fronts, Maximum-likelihood methods (Bond et al., 1998; Wandelt & Hansen, 2003), Gibbs and Bayesian sampling methods (Eriksen et al., 2004; Alsing et al., 2015) are some of the useful methods to estimate full sky CMB angular power spectrum from partial sky spectrum. Hansen et al. (2002) used Gabor transforms for the calculation of full sky CMB angular power spectrum from partial sky spectrum. Another well-known method to estimate full sky CMB angular power spectrum from partial sky spectrum is the so-called pseudo- C_l method (Peebles, 1973; Wandelt et al., 2001; Hivon et al., 2002). Various extensions of this method are specified in Reinecke et al. (2013); Elsner et al. (2016). In this pseudo- C_l technique, the uncertainties of the estimated full sky CMB angular power spectrum are large on lower multipoles due to sample variance that results from the larger fraction of mode loss for lower multipoles. Correlation matrix obtained from pseudo- C_l method also show the high correlations between CMB angular power spectrum of different multipoles. Our ANN becomes very advantageous in such circumstances by avoiding such limitations since the ANN can be trained effectively to learn to recover the lost information due to sky cuts.

Rest of our article is organized as follows. We represent the relation between the ensemble average of full sky and partial sky CMB angular power spectrum in section 2.1. We give a basic description about ANN in section 2.2. In section 3.1 and section 3.2, the detailed procedures of the simulations of full sky and partial sky CMB angular power spectra are given. We discuss, in section 3.3, about the

²<https://pla.esac.esa.int/>

architecture and working procedure of the ANN used by us. We put the results of our work in section 4. In section 4.1, we show the results of the predictions using our ANN model. Significance ratios of the predictions are shown in section 4.2. We describe the results of probability density of predictions in section 4.3. In section 4.4, we discuss about the correlations in the predictions of our ANN model. We present the predictions for observed CMB maps in section 4.5. Finally, we discuss and conclude in section 5.

2 Formalism

2.1 Partial sky to full sky CMB angular power spectrum

Full sky CMB temperature anisotropies, in spherical harmonic space, can be expressed by

$$T(\theta, \phi) - T_0 = \delta T(\theta, \phi) = \sum_{l=0}^{\infty} \sum_{m=-l}^l a_{lm} Y_{lm}(\theta, \phi) \quad (1)$$

where T_0 is the average temperature of CMB radiation, $T(\theta, \phi)$ represents the CMB temperature at a particular position (θ, ϕ) of sky. In the right-hand side of Equation 1, $Y_{lm}(\theta, \phi)$ defines spherical harmonic functions and a_{lm} are harmonic modes of the full sky anisotropies. Harmonic modes (a_{lm}) have $(2l + 1)$ degrees of freedom for a particular l as the index m has the range from $-l$ to l .

From Equation 1, harmonic modes (a_{lm}) can be written as

$$a_{lm} = \int_{\theta=0}^{\pi} \int_{\phi=0}^{2\pi} \delta T(\theta, \phi) Y_{lm}^*(\theta, \phi) d\Omega \quad (2)$$

where $d\Omega$ is the elementary solid angle and $Y_{lm}^*(\theta, \phi)$ defines the complex conjugate of $Y_{lm}(\theta, \phi)$.

Full sky CMB angular power spectrum, from Equation 2, is given by

$$C_l = \frac{1}{2l + 1} \sum_{m=-l}^l |a_{lm}|^2. \quad (3)$$

Equation 3 represents the full sky spectrum which follows the χ^2 distribution with mean C_l^{th} (theoretical CMB angular power spectrum) and variance $2(C_l^{th})^2/(2l + 1)$. We can map the full sky anisotropies in multipoles space using the realizations

of full sky spectrum. The *ensemble average* of the realizations of full sky spectra agrees with theoretical spectrum.

We generate partial sky anisotropy map applying mask on the full sky map. Operation of mask on the full sky map is nothing but the multiplication of a finite window function ($W(\theta, \phi)$) with the full sky anisotropies (Wandelt et al., 2001). So the partial sky anisotropies are given by

$$\delta\tilde{T}(\theta, \phi) = W(\theta, \phi)\delta T(\theta, \phi). \quad (4)$$

Window function, in terms of spherical harmonic functions, is written by

$$W_{lm}^{l'm'} = \int_{\theta=0}^{\pi} \int_{\phi=0}^{2\pi} Y_{l'm'}(\theta, \phi) W(\theta, \phi) Y_{lm}^*(\theta, \phi) d\Omega. \quad (5)$$

Using Equations 1 & 5 in the Equation 4, the harmonic modes of the partial sky anisotropies are expressed by

$$\tilde{a}_{lm} = \sum_{l'=0}^{\infty} \sum_{m'=-l'}^{l'} W_{lm}^{l'm'} a_{l'm'}. \quad (6)$$

The angular power spectrum of this partial sky is defined by

$$\tilde{C}_l = \frac{1}{2l+1} \sum_{m=-l}^l |\tilde{a}_{lm}|^2. \quad (7)$$

We can develop the relation between the *ensemble averages* of the full sky and corresponding partial sky spectra using Equation 3, Equation 6 and Equation 7. So the relation between these two *ensemble averages* is given by

$$\begin{aligned} \langle \tilde{C}_l \rangle &= \sum_{l'=0}^{\infty} \sum_{m=-l}^l \sum_{m'=-l'}^{l'} W_{lm}^{l'm'} \langle C_{l'} \rangle (W_{lm}^{l'm'})^* \\ &= \sum_{l'=0}^{\infty} M_{ll'} \langle C_{l'} \rangle \end{aligned} \quad (8)$$

where the notation $\langle \rangle$ defines the *ensemble average* operator. In Equation 8, $(W_{lm}^{l'm'})^*$ is the complex conjugate of $W_{lm}^{l'm'}$ and $M_{ll'}$ is known as *mode-mode coupling* matrix (Hivon et al., 2002).

Neglecting the instrumental noises at large scales, we can also define the full sky angular power spectrum in terms of corresponding partial sky spectrum, inverting Equation 8, by

$$\langle C_l \rangle = \sum_{l'=0}^{\infty} M_{ll'}^{-1} \langle \tilde{C}_{l'} \rangle. \quad (9)$$

Equation 9 is the fundamental equation of our work. We configure our ANN system to learn this inverse of the *mode-mode coupling* matrix for predicting the full sky angular power spectrum from the corresponding partial sky spectrum.

2.2 Artificial neural network

ANN is a mathematical framework to learn the relation between input data and output data. Let us assume that the output (y), as a function of input (x), can be written as

$$y = f(x). \quad (10)$$

In classical programming, we normally calculate the value of output for a given input value using the relation (Equation 10) between them. In case of ML, usually, we map the relationship between a given set of input data and output data. In Figure 1, we show the block diagram of classical programming and ML.

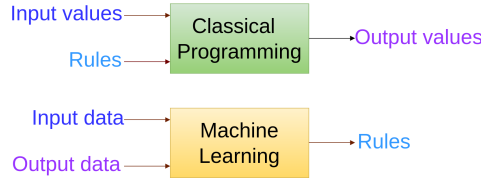


Figure 1: Figure showing the block diagram of classical programming and machine learning (ML). In classical programming, output values are calculated from input values using the relation (rules) between them. ML usually learns the relation (rules) between a given set of input data and output data.

In our case, we employ supervised deep-learning process to predict full sky angular power spectrum using corresponding partial sky spectrum. Deep-learning, using one or more hidden layers in neural network, is a specific subfield of ML. In supervised learning, we train the ANN system using input data as well as *known targets* (output data) to learn the relation between them. Common three types of ML, like *binary classification*, *multiclass classification* and *scalar* or *vector regression*, are interpreted by supervised deep-learning. In present days, the widely

used applications of supervised learning are such as *optical character recognition*, *speech recognition*, *image classification* and *language transition*. In ANN architecture, input layer contains a number of elements which are known as input features. Input layer only provides these input features to the first hidden layer. The major computations are carried by hidden layers and output layer of ANN using randomly initialized *weights* and *biases*.

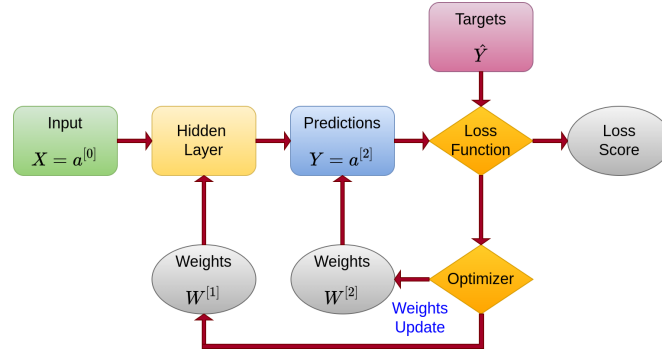


Figure 2: Flowchart of *forward* and *backward* propagation of an *artificial neural network* (ANN) with one hidden layer for *vector regression*. Arrows pointing right from left follow the *forward propagation* process, which takes place from input layer to *loss score* estimation. *Backward propagation* process is indicated by arrows pointing left from right for updating weights and *optimization* processes.

ANN learns the relationship between input data and *known targets* through two processes. One is *forward propagation* and another is known as *backward propagation*. In Figure 2, we show a flowchart of *forward* and *backward propagation* processes of an ANN with one hidden layer. Let us define the input features as X , a column matrix. Number of elements (x_i) of this column matrix is equivalent to the number of neurons in the input layer. In ANN architecture, each neuron of a particular layer connects all neurons of the previous layer by *weights*. We denote the matrix representation of *weights* by $W^{[p]}$, where superscript $[p]$ defines the p -th layer. It is a two dimensional matrix which has the number of columns and rows same as the number of neurons in present layer and the previous layer. We define the matrix representation of *biases* by $b^{[p]}$, a column matrix, for the p -th layer. *Bias* matrix contains the number of elements equivalent to the number of neurons of the present layer. Moreover, we need to define a *activation function*, denoted by $a^{[p]}$ for p -th layer, to learn the non-linearity in each layer except input layer. In input layer (0-th layer), $a^{[0]}$ defines the input features (X). *Activation function* in output layer is simply a linear function for *regression* problems. Now

the mathematical representations of *forward propagation* can be expressed by

$$z_i^{[p]} = \sum_{j=0}^{n^{[p-1]}} w_{ij}^{[p]} a_j^{[p-1]} + b_i^{[p]} \quad (11)$$

$$a_i^{[p]} = g^{[p]}(z_i^{[p]}) \quad (12)$$

where $n^{[p]}$ is the number of neurons in p -th layer. In Equation 11, $z_i^{[p]}$ represents the linear part of i -th neuron in p -th layer and in Equation 12, $g^{[p]}$ defines the specific *activation function*. We use non-linear *activation function* (e.g., *sigmoid*, *tanh*, ReLU, LeakyReLU) in the hidden layers to learn the non-linearity between the given input and *target* data set. In *scalar* or *vector regression* problems, we choose identity *activation function* for output layer since the prediction values are real numbers. So the prediction values in the output layer can be written as

$$y_q = a_q^{[P]} = z_q^{[P]} = \sum_{j=0}^{n^{[P-1]}} w_{qj}^{[P]} a_j^{[P-1]} + b_q^{[P]} \quad (13)$$

where superscript $[P]$ specify the output layer and y_q defines the q -th prediction of the output layer. We show the architecture of an ANN with one hidden layer for *vector regression* problem in Figure 3. In input layer ($p = 0$), $a_i^{[0]}$ are the input features (x_i) of ANN, where $i = 0, 1, \dots, n^{[0]}$. In the hidden layer ($p = 1$), $z_j^{[1]}$ are calculated by Equation 11 and $a_j^{[1]}$ are obtained from Equation 12, where $j = 0, 1, \dots, n^{[1]}$. In the output layer ($P = 2$), $z_q^{[2]}$ and $a_q^{[2]}$ are calculated by Equation 13, where predictions $y_q = a_q^{[2]} = z_q^{[2]}$, for $q = 0, 1, \dots, n^{[2]}$. This is the *forward propagation* part up to estimating *loss score*, using *loss function* (e.g., common *loss function* like *mean squared error* (MSE) for *regression*), between predictions and *known targets* in output layer. MSE *loss function* can be expressed by

$$L^{MSE} = \frac{1}{n^{[P]}} \sum_{q=0}^{n^{[P]}} (y_q - \hat{y}_q)^2 \quad (14)$$

where \hat{y}_q is q -th *known target* for a particular sample and $n^{[P]}$ represents the number of neurons in the output layer. We use multiple samples of inputs (X^k) and *targets* (\hat{Y}^k) to train ANN, where superscript k defines k -th sample and $k = 0, 1, \dots, m$. The *cost function* (J^{MSE}), for MSE *loss function*, is defined by

$$J^{MSE} = \frac{1}{m} \sum_{k=0}^m L_k^{MSE}. \quad (15)$$

ANN calculates the *loss score*, value of *cost function*, through the *forward propagation* using Equation 15. Reaching to the minimum value of *loss score* signifies ANN is trained very well.

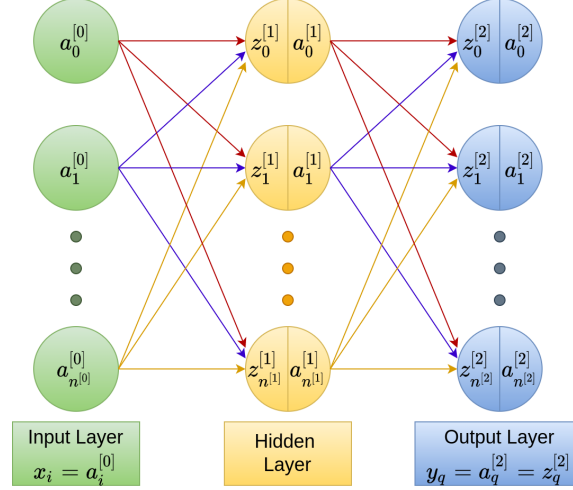


Figure 3: Architecture of ANN with one hidden layer for *vector regression*, where $n^{[p]}$ defines the number of neurons in p th layer. We show two parts in the circle (neurons of the layer) of hidden layer and output layer, where $z_j^{[p]}$ is linear part and $a_j^{[p]}$ is *activation function* for j th neuron in p th layer. In input layer, x_i are the input features given by us. In output layer, y_q are the predictions from the ANN system.

We use *backward propagation* algorithm in ANN to minimize the value of *cost function* (Hecht-Nielsen, 1992). In *backward propagation*, *weights* and *biases* are updated by *optimization* process using a particular *optimizer* (e.g., *stochastic gradient descent* (SGD), *momentum*, *adaptive moment estimation* (ADAM ; Kingma & Ba (2014)), RMSProp (Hinton et al., 2012)). ANN calculate the gradients of *cost function* (J) with respect to *weights* (w_{ij}) and *biases* (b_i) through the *optimization* process (Sun et al., 2020). These gradients can be written by

$$\delta w_{ij} = \frac{\partial J}{\partial w_{ij}}. \quad (16)$$

$$\delta b_i = \frac{\partial J}{\partial b_i}. \quad (17)$$

The *optimization* process utilizes the gradients of *cost function*, defined in Equation 16 and Equation 17, to reconstruct *weights* from w_{ij} to $w_{ij} - \alpha \delta w_{ij}$ and *biases* from b_i to $b_i - \alpha \delta b_i$, where α is *learning rate* hyperparameter of the *optimizer*.

After updating of *weights* and *biases*, ANN calculates the *cost function* through *forward propagation* again in each iteration. These two processes help minimize the *cost function* for accurate training of the ANN system.

Estimation of uncertainties is a crucial point for data analysis in cosmology. So it will be more efficient if we are able to measure uncertainties for corresponding predictions in supervised deep-learning regression problem. We encounter two types of uncertainties in ML. One is *aleatoric* uncertainty and another is *epistemic* uncertainty (Kendall & Gal, 2017). *Aleatoric* uncertainties appear due to the inherent noises in data. Though we can't remove these *aleatoric* uncertainties from ANN, it can be measured using *heteroscedastic* loss function for *vector regression* problem. The *heteroscedastic* (HS) loss function (Kendall & Gal, 2017) can be defined by

$$L^{HS} = \frac{1}{2n^{[p]}} \sum_{q=0}^{n^{[p]}} [\exp(-s_q) (y_q - \hat{y}_q)^2 + s_q] \quad (18)$$

where s_q is the log variances $\ln(\sigma_q^2)$ and σ_q is the *aleatoric* uncertainties for corresponding prediction values (y_q). *Epistemic* uncertainties exist in ANN due to a lack of knowledge in data as well as ignorance about model parameters. We can reduce it by taking more data samples to train ANN. We can also use one of the various techniques like *model averaging ensemble* (Lai et al., 2021), *bootstrapping*, *concrete dropout* (Gal et al., 2017) to minimize *epistemic* uncertainties.

3 Methodology

HEALPix³ (Gorski et al., 2005) is a widely used software for simulations in cosmology. It is available in many programming languages (C, C++, IDL, Fortran, Python). We use the Python version of this software (healpy⁴) in our simulations. We take the theoretical CMB angular power spectrum (C_l^{th}), from Planck Collaboration VI (2020) for the purpose of simulations. We present the cosmological parameters, calculated by Planck Collaboration VI (2020), in Table 1. We also use TensorFlow⁵ (Abadi et al., 2015) ML platform to create ANN and to train that ANN for supervised deep-learning of *vector regression*.

³<https://healpix.sourceforge.io/>

⁴<https://github.com/healpy/healpy>

⁵<https://www.tensorflow.org/>

Table 1: Cosmological parameters obtained by [Planck Collaboration VI \(2020\)](#) from standard Λ CDM model with a power law spectral index, where Ω_b is today's baryonic density parameter, Ω_c is today's density parameter of cold dark matter, H_0 is today's Hubble parameter in units of $km/s/Mpc$, τ is optical depth to decoupling surface, n_s is scalar spectral index and A_s is the characterize parameter for the amplitude of initial perturbations.

Parameter	Value
$\Omega_b h^2$	0.022 ± 0.0001
$\Omega_c h^2$	0.12 ± 0.001
H_0	67.37 ± 0.54
Ω_k	0.001 ± 0.002
τ	0.054 ± 0.007
n_s	0.965 ± 0.004
$\ln(10^{10} A_s)$	3.043 ± 0.014

3.1 Simulations of full sky CMB angular power spectra

We generate full sky CMB temperature anisotropy ($\delta T(\theta, \phi)$) map from theoretical CMB angular power spectrum (C_l^{th}) with a maximum multipole (l_{max}). We work with resolution parameter $N_{side} = 256$ and corresponding pixel window function (\mathcal{P}_l), provided by HEALPix software package, for the generation of full sky map. We use $l_{max} = 3N_{side} - 1 = 767$ to obtain the full sky maps using randomly chosen seed values. Let us define a notation D_l for CMB angular power spectrum multiplied by $l(l+1)/2\pi$. In Figure 4, we show the curve of theoretical D_l^{th} in μK^2 unit for the multipole range $2 \leq l \leq 767$. We ignore monopole ($l = 0$) and dipole ($l = 1$) power since they do not give any cosmological information. In the top panel of Figure 5, we show the mollweide projection of full sky map for a randomly selected seed value.

Number of pixels, for a particular N_{side} , can be written as

$$N_{pix} = 12 \times N_{side}^2. \quad (19)$$

Angular resolution (N_{res}), for that specific N_{side} , can be expressed by

$$N_{res} = \left[\sqrt{\frac{4\pi}{N_{pix}}} \frac{180}{\pi} \right]^\circ. \quad (20)$$

So we can calculate, using Equation 19 and Equation 20, the angular resolution 13.74 arcmin for $N_{side} = 256$.

We obtain pixel-smoothed full sky spectrum (C_l^{pix}), using ring weighting and $l_{max} = 2N_{side} = 512$, from full sky map. For strictly band-width limited functions, the maximum multipole range $2N_{side} < l_{max} < 3N_{side} - 1$ can be easily

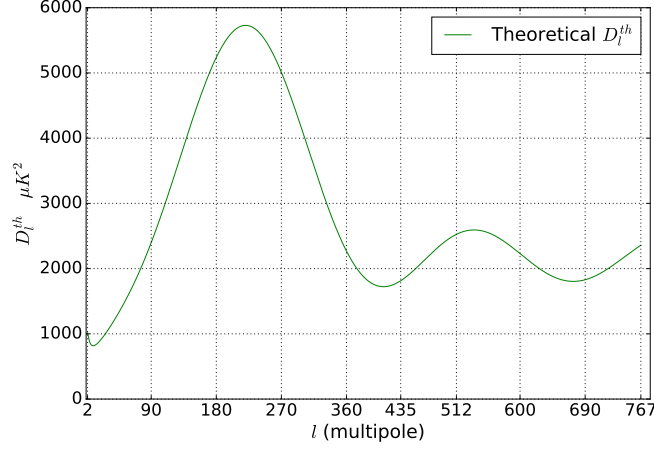


Figure 4: Figure showing the theoretical angular power spectrum $D_l^{th} = l(l+1)C_l/2\pi$ (Planck Collaboration VI, 2020) used to simulate the random realizations of CMB maps for the multipole range $2 \leq l \leq 767$.

managed. We use $l_{max} = 2N_{side} = 512$ to generate the full sky pixel-smoothed spectrum and $l_{max} = 3N_{side} - 1 = 767$ for obtaining partial sky pixel-smoothed spectrum. These selections of maximum multipole help our ANN system to take more information, as input features, for learning the inverse of *mode-mode coupling* matrix beneficially. If we take l_{max} as $2N_{side}$ or $3N_{side} - 1$ for generating angular power spectrum for both full sky and partial sky, then ANN system will suffer from a lack of knowledge in input features to predict the full sky spectrum with same dimension as of input features.

Finally, we divide the pixel-smoothed full sky spectrum by the square of corresponding pixel window function to find the full sky spectrum (C_l). Bottom panel of Figure 5 shows the realization of full sky D_l in μK^2 unit, corresponding to the full sky map shown in the top panel of Figure 5, for the multipole range $2 \leq l \leq 512$. We can produce a number of realizations of full sky maps from C_l^{th} using randomly selected seed values and generate same number of realizations of C_l from these full sky maps. Ensemble average of these realizations of C_l agrees with the theoretical spectrum. Using a large number of simulations helps achieve higher accuracy of the agreement by suppressing any possible residual Monte-Carlo noise in the ensemble averaged spectrum.

3.2 Simulations of partial sky CMB angular power spectra

We produce partial sky CMB temperature anisotropy map after applying WMAP Kp2-mask⁶ (Bennett et al., 2003) on the full sky CMB map. Kp2-mask is available

⁶<https://lambda.gsfc.nasa.gov/product/map/drl/imask.cfm>

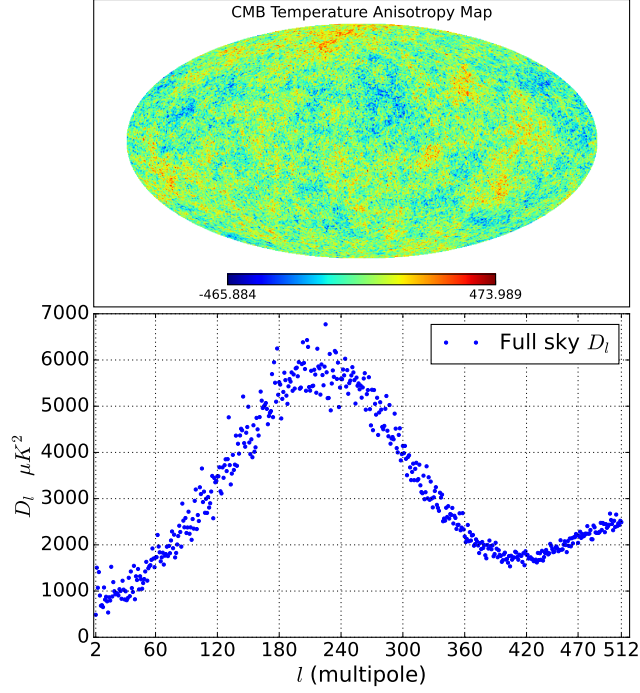


Figure 5: Top panel shows the full sky CMB temperature anisotropy map, simulated from theoretical CMB angular power spectrum (C_l^{th}) with $l_{max} = 767$, for a randomly selected seed value. The bottom panel represents the corresponding full sky $D_l = l(l + 1)C_l/2\pi$ in μK^2 , calculated from full sky map for $l_{max} = 512$.

with pixel resolution $N_{side} = 512$. For the purpose of our analysis we downgrade it to $N_{side} = 256$. The degradation of pixel resolution causes some pixels of the mask at lower resolution to have fractional values between 0 and 1. We convert this downgraded mask to a binary mask by modifying the fractional pixel values. This is achieved by assigning all pixels of the mask originally with values larger than 0.5 to the new value of unity. We assign the rest of the pixel values of the mask to the value 0. We apply this binary mask on the full sky CMB maps. Such masking is essential to remove any possible (residual) foreground contaminations arising due the galactic region and extragalactic bright point sources before cosmological analysis in case foreground cleaned CMB maps. In Figure 6, we show the mollweide projection of this binary Kp2-mask.

We obtain partial sky spectra (\tilde{C}_l^{pix}) using the input partial sky maps obtained above. We use ring weighting with $l_{max} = 3N_{side} - 1 = 767$ for the generation of \tilde{C}_l^{pix} which will be served as input to the ANN. This helps to provide the ANN with as much spectral information as possible within the limits of numerical algorithms used to perform spherical harmonic transformations. We note that these partial sky spectra contain pixel smoothing effects since the input full sky CMB

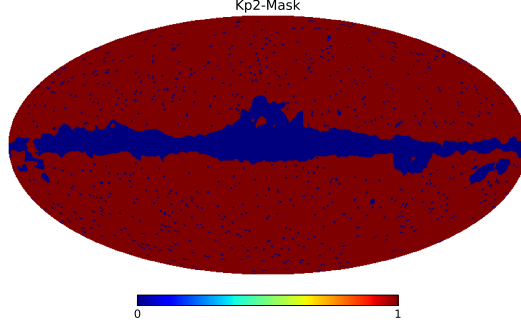


Figure 6: Mollweide projection of the Kp2-mask used in this work at $N_{side} = 256$. Note that the mask removes both the galactic region and positions of the extragalactic bright point sources. For details of construction of the mask, we refer to section 3.2.

maps are smoothed by the pixel window function.

Finally, we scale the smoothed partial sky spectrum (\tilde{C}_l^{pix}) by dividing by the square of the pixel window function to obtain a scaled spectrum (\tilde{C}_l). We generate 1.5×10^5 number of realizations of partial sky $\tilde{D}_l = l(l+1)\tilde{C}_l/2\pi$. In Figure 7, top panel shows the partial sky CMB temperature anisotropy map for a randomly chosen seed value. The bottom panel represents the corresponding partial sky \tilde{D}_l in μK^2 unit for the multipole range $2 \leq l \leq 767$. Comparing the bottom panels of Figure 5 and Figure 7, we notice that the power of the partial sky spectrum is less compared to the full sky case. This is expected since application of mask removes some fractions of independent numbers of modes at each angular scales.

3.3 ANN for our analysis

We use *sequential* model and *dense* layer (densely connected layer) from *keras* library of TensorFlow ML platform in our supervised deep-learning *vector regression* problem. We create an ANN with input layer, one hidden layer (contained ReLU *activation* function) and output layer (carried identity *activation* function). We utilize L_2 *kernel regularizer*, with a factor 10^{-3} , in the hidden layer to avoid any possible overfitting in our ANN system. We use the realizations of partial sky \tilde{D}_l , for the multipole range $1 \leq l \leq 767$, as input data \mathbf{X}^k with matrix elements x_i^k , where $i = 0, 1, \dots, 766$ and superscript k defines the k -th sample. We take the realizations of full sky D_l , for the multipole range $2 \leq l \leq 512$, as known targets $\hat{\mathbf{Y}}^k$ with matrix elements y_q^k , where $q = 0, 1, \dots, 510$ and superscript k represents the k -th sample. We create 1.5×10^5 number of samples of full sky D_l and partial sky \tilde{D}_l . We use first 80% samples of the set for training. From the rest of the samples, we use first half for validation and last half for testing the performance

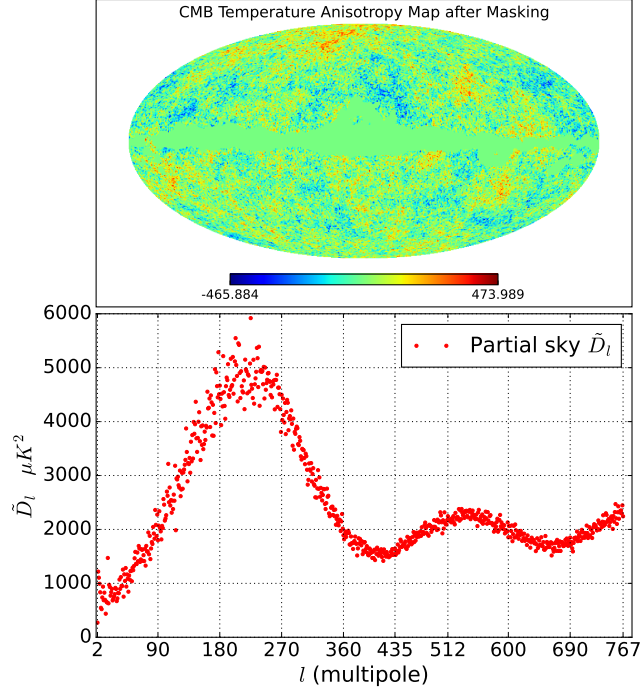


Figure 7: Top panel shows the partial sky CMB temperature anisotropy map obtained by masking the full sky simulated CMB map using theoretical CMB angular power spectrum (C_l^{th}), given by [Planck Collaboration VI \(2020\)](#), with $l_{max} = 767$ using a randomly chosen seed value. Bottom panel shows the corresponding partial sky $\tilde{D}_l = l(l+1)\tilde{C}_l/2\pi$ in μK^2 unit, calculated from partial sky map of the top panel, for the multipole range $2 \leq l \leq 767$. Reduction of power due to masking can be concluded by comparing this figure with the bottom panel of Figure 5.

of our ANN system. We make use of *heteroscedastic* loss function (L^{HS}), defined in Equation 18, in our ANN system for predicting output values as well as corresponding *aleatoric* uncertainties. So the number of neurons in input layer ($n^{[0]}$) is equal to 767 and the number of neurons in output layer ($n^{[2]}$) is equivalent to 1022. The first half of the output layer ($0 \leq q \leq 510$) determines the predictions and last half of the output layer ($511 \leq q \leq 1021$) gives the log variances (s_q) of corresponding predictions. The number of neurons in the hidden layer ($n^{[1]}$) is calculated by a simple average of number of neurons in the input and the output layers. We take this number to be ≈ 895 for our case. In Figure 8, we show a schematic diagram of our ANN system contained one hidden layer as well as *heteroscedastic* loss function (L^{HS}).

Preprocessing of input data is a well-known procedure in ML. This procedure arranges the input data with a better scaling to train an ANN effectively. We

perform the preprocessing using *standardization* method for scaling the input data \mathbf{X}^k with mean 0 and standard deviation 1. We take the mean as well as the standard deviation of the training samples. Then, each sample is subtracted by the mean and divided by the standard deviation. This *preprocessing* is also applied to the validation set and test set. We standardize the validation and test sets by using the mean and standard deviations of samples obtained from the training set. This helps to effectively pass on the information learnt by the ANN during the training process for predictions in the validation and test cases. We also scale the known targets $\hat{\mathbf{Y}}^k$, dividing by 10^3 , to decrease the range of values of $\hat{\mathbf{Y}}^k$. This helps the ANN system to learn easily and quickly.

A common problem of an ANN system is that it can be trapped at a local minimum of the loss function (in our case it is L^{HS}). We employ mini-batch *optimization* algorithm (e.g., *mini-batch stochastic gradient descent* (MSGD), ADAM etc.) to overcome this local minima problem (Ruder, 2016). We operate our ANN system with ADAM *optimizer*, where we set *learning rate* hyperparameter $\alpha = 10^{-4}$ for tuning our ANN system. In mini-batch *optimization* algorithm, ANN system uses a subset from entire training set for each iteration. Completing all iterations, ANN is trained with the entire training set. To decide how many times the *optimization* process should go on we use 200 *epochs*. We also fix the mini-batch size (m_b) conveniently to a value of 2048 which is less than the number of entire training samples (m). So the number of iterations, in each epoch, will be $m/m_b = 59$.

After training our ANN system with training samples, we predict the full sky D_l , for the multipole range $2 \leq l \leq 512$, using input data (\tilde{D}_l) of 1.5×10^4 test samples. As we use *heteroscedastic* loss function (L^{HS}), we get predictions (y_q) as well as log variances (s_q) of corresponding predictions from the same ANN system. We calculate aleatoric uncertainties (σ_q) taking the square root of $\exp(s_q)$. We generate random Gaussian realizations from the Gaussian distribution with 0 mean value and σ_q as the standard deviation (Chanda & Saha, 2021). So the final results of the full sky D_l are the sum of predicted full sky D_l , for the multipole range $2 \leq l \leq 512$, and these Gaussian realizations. Chanda & Saha (2021) used *concrete dropout* (Gal et al., 2017) to minimize the *epistemic* uncertainties of their ANN system for $N_{side} = 16$ case. We note in passing that using *model averaging ensemble* method as used in this work requires less computational resources compared with the alternative approach of computing *epistemic* uncertainties using the so-called *concrete dropout* of the neurons.

Here, we discuss the ability of *model averaging ensemble* method (Lai et al., 2021) to minimize the *epistemic* uncertainties of our ANN system to avoid the computational cost. For this method, we concentrate on the random initialization of *weights* ($\mathbf{W}^{[p]}$) and *biases* ($\mathbf{b}^{[p]}$) in *dense* layer. Output of ANN will change

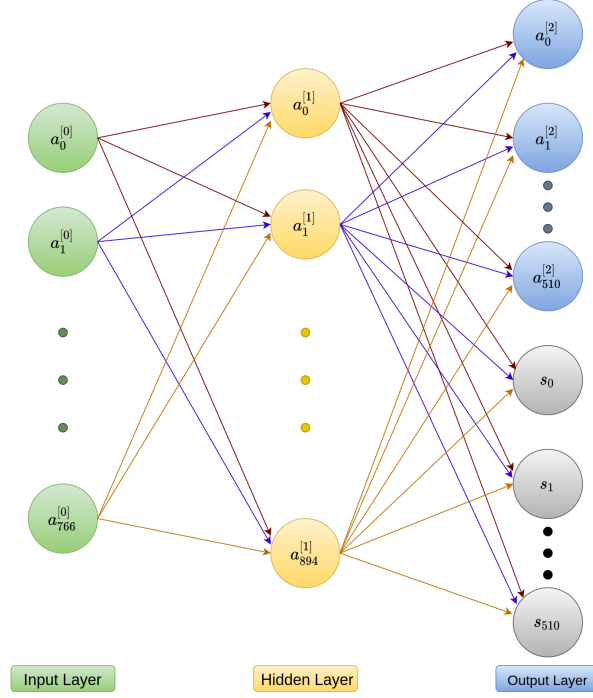


Figure 8: Architecture of our ANN system with one hidden layer for *heteroscedastic* loss function. In the input layer, $a_i^{[0]}$, where $i = 0, 1, \dots, 766$, represents the input features. In the hidden layer, $a_i^{[1]}$, where $i = 0, 1, \dots, 894$, are the values of ReLU activation function. First half of output layer represents the predictions (y_q) and second half of the output layer represents the log variances (s_q) of the predictions (y_q), where $q = 0, 1, \dots, 510$.

depending upon the random initialization of $\mathbf{W}^{[p]}$ and $\mathbf{b}^{[p]}$. We train the same ANN system, with same hyperparameter and same tuning, for a total of 50 times for 50 randomly chosen seed values using TensorFlow library. Then, we find the final predictions (y_q^{mean}) taking the simple mean of these 50 output sets. For the estimation of corresponding *aleatoric* uncertainties (σ_q^{rms} ; *rms* stands for root mean square), at first we calculate exponential of log variances (s_q) for each of 50 output sets. Thereafter, we take the simple mean of $\exp(s_q)$ from these 50 output sets, and the final *aleatoric* uncertainties (σ_q^{rms}) are obtained by taking square root of the mean values of $\exp(s_q)$. Finally, we obtain the full sky D_l by computing the sum of mean predictions (y_q^{mean}) and the random Gaussian realizations created from Gaussian distributions with 0 mean and σ_q^{rms} standard deviation. Thus, we get accurate results from our ANN system minimizing the *epistemic* uncertainties. The entire set of 50 iterations of training of our ANN system were performed

using Google Colab⁷, a platform for an efficient online GPU service offered by Google for the purpose of ML. It takes approximately 3 hours 45 minutes to perform the entire set of training.

4 Results

4.1 Predictions of full sky D_l

We use a total of 1.5×10^4 test samples of partial sky CMB spectra to predict the corresponding full sky spectrum for each of the test cases. We predict the realizations of full sky D_l for the multipole range $2 \leq l \leq 512$ using our trained ANN architecture. We show the predicted and target full sky D_l in Figure 9 for four different randomly chosen test samples. Both the predicted and target spectra agree very well with each other within a small level of random fluctuations in each of the sub-figures. We assess any possible bias in the samples of predicted full sky spectrum by computing of the mean spectrum for the predicted and target sets of D_l . We show the mean predicted full sky spectrum (D_l^{pred}) and the mean target full sky spectrum (D_l^{true}) using the test samples in the top panel of Figure 10. These two spectra overlap with each other which completely indicates an excellent agreement between the two. This shows that our ANN can construct unbiased estimators of the full sky CMB spectra. The theoretical spectrum (D_l^{th}) is also shown in this figure with the dashed green line for comparison. The predicted samples also preserve the underlying two-point correlations. We show this by comparing the standard deviations of D_l computed from the predicted and target test samples in the bottom panel of Figure 10. Again the standard deviations for each multipole agree very well with each other and with the cosmic variance error which is shown in green line.

4.2 Significance ratios

To assess the effectiveness and accuracy of the predictions of ANN we estimate the significance ratio of the predicted full sky spectrum D_l . We first calculate the differences between the mean predicted and (mean) *target* spectra for each multipole. We obtain the standard error of mean (SEM) predicted spectra by computing the standard deviation divided by the square root of the number of *target* test samples, for each multipole. Then, we take the ratios between those differences and these SEM of full sky target D_l , for every multipole. We find that these significance ratios lie entirely within 3σ , at each multipole. This indicates that our ANN system predicts accurately and there is no significant bias in the predicted full sky

⁷https://colab.research.google.com/?utm_source=scs-index

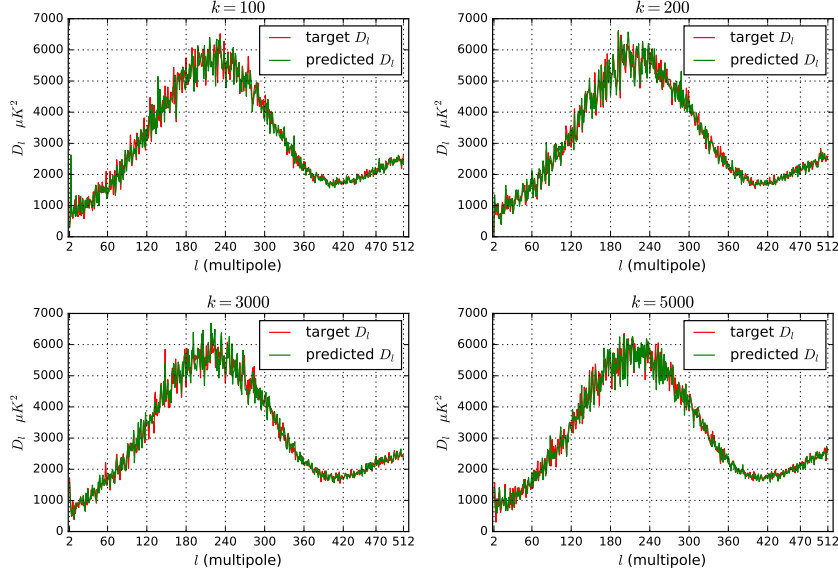


Figure 9: Figure showing the predicted (green) and target (red) full sky $D_l = l(l+1)C_l/2\pi$ for four randomly selected samples with random seeds as indicated above each of the sub-figures. As we see from these sub-figures the predicted and target full sky angular spectra agree very well with each other demonstrating that the ANN has learned the specific realization mapping between the partial sky and the corresponding full sky angular power spectrum.

spectra. In Figure 11, we show the significance ratios of the predicted D_l for every multipole. Horizontal dashed green lines define the 3σ error interval. The *model averaging ensemble* (Lai et al., 2021) method effectively minimizes the epistemic uncertainties of our ANN system.

4.3 Probability density

We verify that the predicted D_l at every multipole follows χ^2 distributions as we expect from the Gaussian nature of CMB anisotropies. We obtain the probability density of predicted D_l as well as the target D_l by finding normalized histograms for each multipole. We also calculate the conditional probability densities of full sky CMB angular spectra given theoretical D_l^{th} (Sudevan & Saha, 2020), for every multipole. We present the normalized histograms in Figure 12 for some different multipoles. Horizontal axis of each sub-figure represents the values of full sky D_l in $1000\mu K^2$ unit. Normalized histograms show that the probability densities of predicted D_l agree very well with the probability densities of target D_l for each multipole. These normalized histograms also agree with the theoretical probability densities excellently. So the predicted full sky spectrum from our ANN system

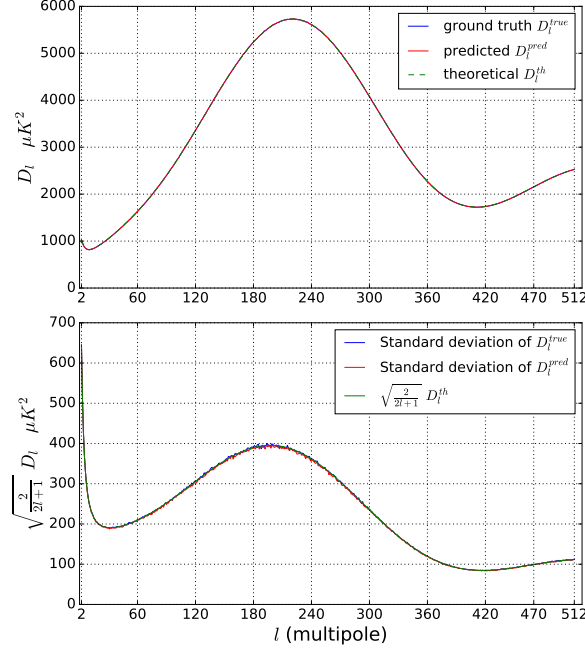


Figure 10: Top panel of the figure shows the mean curves of ground truth (red), predicted (blue) and theoretical (green) full sky $D_l = l(l + 1)C_l/2\pi$ in μK^2 for the multipole range $2 \leq l \leq 512$. The mean predicted spectrum (blue) is completely consistent with the ground truth (red) and theoretical (green) spectrum. Bottom panel shows the corresponding standard deviation curves of ground truth (red), predicted (blue) and theoretical (green) D_l in μK^2 for the same multipole range. The predicted (red) standard deviation curve also agrees very well with the standard deviation curves of ground-truth (blue) and theoretical (green) spectrum.

preserves the statistics of χ^2 distribution very nicely.

4.4 Correlation matrix

We estimate the multipole-space correlation matrix for the predicted full sky spectra for the multipole range $2 \leq l \leq 512$ to investigate any possible correlations that may exist in our predictions. We show this correlation matrix in Figure 13. As we see from this figure the correlation matrix is dominantly diagonal. We clip the colour bar in the range ± 0.15 to zoom in the off-diagonal elements of the matrix. We note that the values of the off-diagonal elements of the correlation matrix range entirely within ± 0.04 . Therefore the correlation matrix obtained from predicted full sky spectra indicates that the predictions from our ANN system do not cause any significant correlation between the power of different multipoles. This is yet another attractive feature of the ANN predictions used in our work. Our

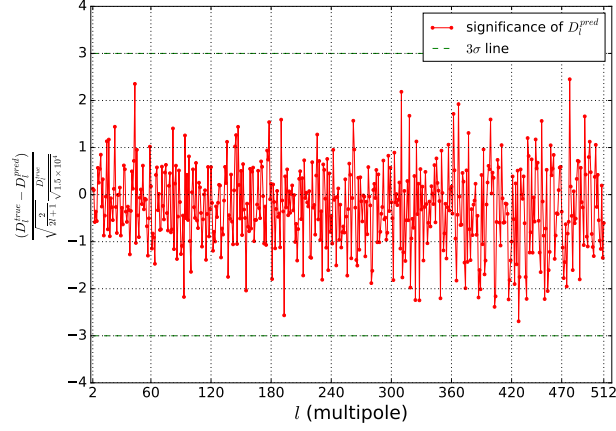


Figure 11: Significance ratios of the predicted $D_l = l(l+1)C_l/2\pi$ for the multipole range $2 \leq l \leq 512$. The figure shows all points (red) are entirely within a 3σ error interval (dashed green line).

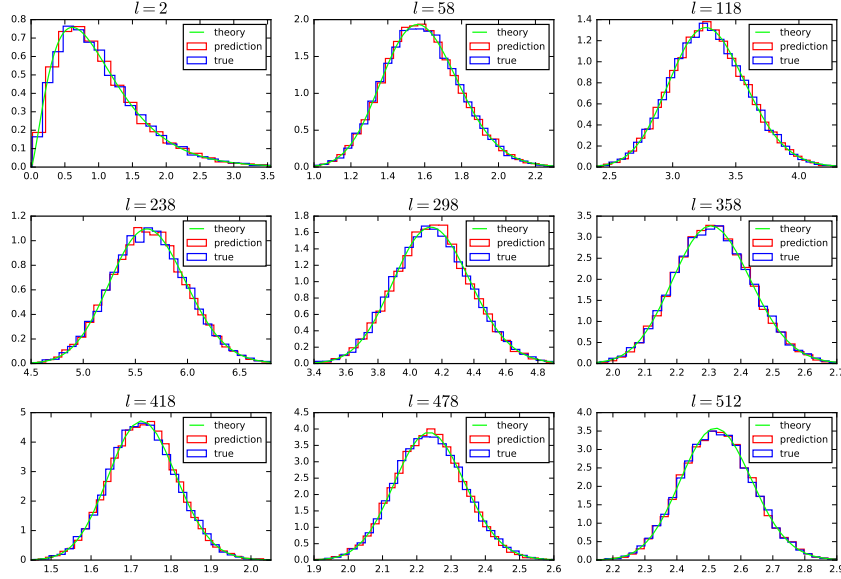


Figure 12: Every sub-figure shows the probability density (normalized histogram) of predicted (red) and target (blue) $D_l = l(l+1)C_l/2\pi$ as well as the conditional probability density (lime) of full sky (given theoretical spectrum) for different multipoles. Predicted (red) probability densities give an excellent agreement with target (blue) and theoretical (lime) probability densities. Horizontal axis of each sub-figure represents full sky D_l in $1000\mu K^2$ unit.

ANN can produce nearly correlation free predicted spectra by effectively filtering out the multipole correlations that exist in the partial sky spectra due to *mode-*

mode coupling.

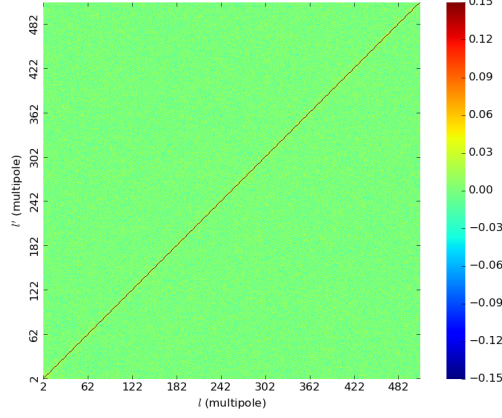


Figure 13: Figure shows the correlation matrix of our predicted $D_l = l(l + 1)C_l/2\pi$ for the multipole range $2 \leq l \leq 512$. The values of diagonal elements of the matrix are unity. We clip the colour bar within ± 0.15 to zoom in the off-diagonal regions. The maximum and minimum values of the off-diagonal elements lie within ± 0.04 .

4.5 Predictions for observed CMB maps

We further apply our ANN system, trained with 1.2×10^5 training samples, on the available unpainted foreground cleaned CMB maps. We collect these CMB maps (e.g., COMMANDER, NILC, SMICA and SEVEM)⁸ from [Planck Collaboration IV \(2020\)](#). We apply Kp2-mask, for $N_{side} = 256$, on these four unpainted full sky maps. We obtain the partial sky spectra using these four unpainted partial sky maps for maximum multipole $l_{max} = 767$. We use these unpainted partial sky \tilde{D}_l as input data to predict corresponding full sky D_l , up to maximum multipole $l_{max} = 512$, using our ANN architecture.

We use inpainted full sky spectra for comparing the consistency of predictions of our ANN system on Planck data ([Planck Collaboration IV, 2020](#)). These inpainted spectra are obtained from four inpainted CMB intensity maps (e.g., COMMANDER, NILC, SMICA and SEVEM), provided by Planck mission. Inpainted maps are generated by [Planck Collaboration IV \(2020\)](#) from unpainted foreground cleaned CMB maps replacing some pixels of galactic plane, very bright sources and extragalactic point sources regions by a sample realization drawn from the posterior distribution given the un-masked pixels. The method preserves the statistical properties of the entire even after infilling some regions of the sky. Interest-

⁸<https://pla.esac.esa.int/>

ingly, the predictions from our exercise, shown in Figure 14, exhibit an excellent agreement with theoretical spectrum as well as the inpainted full sky D_l obtained from inpainted CMB maps (Planck Collaboration IV, 2020).

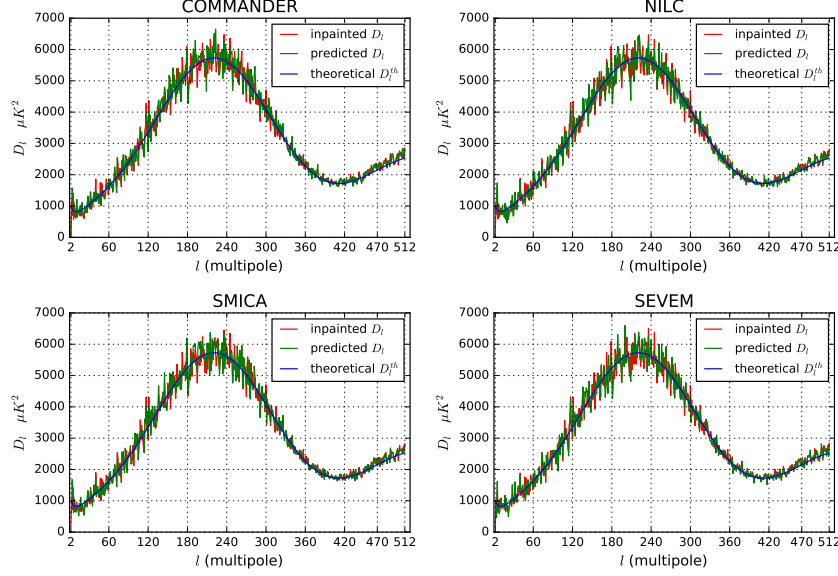


Figure 14: Figure shows the excellent agreement of the predicted (green) $D_l = l(l + 1)C_l/2\pi$ and inpainted (red) D_l , for COMMANDER, NILC, SMICA and SEVEM, in the multipole range $2 \leq l \leq 512$. Predicted (green) spectra also agree with the theoretical (blue) spectrum excellently shown in the same graph.

5 Discussions and Conclusions

Accurate estimation of full sky CMB angular power spectrum (C_l), from CMB map after masking off some finite regions, may be a problem of utmost importance for reliable extraction of cosmological information from the observed CMB maps. For large pixel array data, as is the case for high resolution CMB maps, the available methods can be computationally expensive (e.g., the exact maximum likelihood approach) or may not be optimal (e.g, over large angular scales and limited by sample variance). In such cases, training an artificially intelligent system seems to be an effective alternative method which can produce optimal results with the requirements of only a small amount of available computing resources. In the current work, we evolve the earlier work of Chanda & Saha (2021) for $N_{side} = 16$, to predict the full sky CMB angular power spectrum using ANN after application of Kp2-Mask using $N_{side} = 256$ HEALPix maps and

up to $l_{max} = 512$. The mask removes both the (strongly contaminated) galactic plane and the positions of extragalactic bright point sources as required by a high resolution CMB analysis.

The major advantages of our predicted full sky spectrum are summarized below.

(i) Our ANN is designed to predict the full sky estimates for any random realization of the CMB map which agrees well with the target spectrum within a small amount of random differences.

(ii) The predictions are achieved at each multipole. This is a great advantage since we can avoid the requirements of any binning for whatsoever purposes (e.g., reducing scatter or correlation that is otherwise needed since the non-intelligent systems can in no way learn to get back the lost information after masking.)

(iii) The predicted spectra preserve the statistical properties of the target spectra. This means that the predicted power spectrum at each multipole is unbiased, preserves the cosmic variance error, follows the identical distributions as the target full sky spectrum and shows no correlations between the power spectrum estimates of any two different multipoles. The conservation of underlying density functions in predicted and target spectra open up a further window to utilize the predicted spectrum for cosmological parameter estimation in a reliable fashion.

Our ANN consists of one hidden layer and takes only about 3 hours 45 minutes on GPU, for predicting full sky D_l for $l_{max} = 512$. The ANN predicts both the full sky spectra and the corresponding cosmic variance induced error at each multipole. We use *model averaging ensemble* methods to minimize the epistemic error. Using a sufficiently generous mask in our analysis, we find that the mean of the predicted full sky spectra agrees within 3σ (99.7% confidence level) with the underlying theoretical spectrum indicating the predictions are unbiased. On applying our trained ANN on the partial sky (Kp2 masked) maps generated from unpainted foreground cleaned CMB maps, COMMANDER, NILC, SMICA and SEVEM, we find an excellent agreement of predicted spectra with the corresponding full sky spectra from cleaned (inpainted) maps ([Planck Collaboration IV, 2020](#)). This again shows that our ANN has learnt to reconstruct the lost information due to masking reliably based upon the training. In a future article we will utilize ANN in the problem of CMB component separation over partial sky so as to reconstruct the joint distributions of (partial sky) cleaned CMB map and the corresponding full sky spectrum.

Acknowledgements

Authors acknowledge the use of the open-source packages HEALPix⁹, TensorFlow¹⁰ and Google Colab¹¹.

References

- Abadi M., et al., 2015, TensorFlow: Large-Scale Machine Learning on Heterogeneous Systems, download.tensorflow.org/paper/whitepaper2015.pdf
- Acquaviva, V., Bartolo, N., Matarrese, S. and Riotto, A., 2003, *Nuclear Physics B*, **667**, 119
- Allen, T. J., Grinstein, B., and Wise, M. B., 1987, *Physics Letters B*, **197**, 66
- Alsing J., Heavens A., Jaffe A. H., Kiessling A., Wandelt B., Hoffmann T., 2015, *MNRAS*, **455**, 4452
- Baccigalupi C., Bedini L., Burigana C., de Zotti G., Farusi A., Maino D., Maris M., Perrotta F., Salerno E., Toffolatti L. and Tonazzini A., 2000, *MNRAS*, **318**, 769
- Bennett C. L. et al., 1996, *ApJ*, **464**, L1
- Bennett C. L. et al., 2003, *ApJS*, **148**, 97
- Bond J. R., Jaffe A. H., Knox L., 1998, *Phys. Rev. D*, **57**, 2117
- Chanda P. and Saha R. 2021, *MNRAS*, **508**, 4600
- Dialektopoulos K., Said J. L., Mifsud J., Sultana J. and Adami K. Z., 2021, arxiv.org/abs/2111.11462
- Elsner F., Leistedt B., Peiris H. V., 2016, *MNRAS*, **465**, 1847
- Eriksen H. K., O’Dwyer I. J., Jewell J. B., Wandelt B. D., Larson D. L., Gorski K. M., Levin S., Banday A. J. and Lilje P. B., 2004, *ApJS*, **155**, 227
- Escamilla-Rivera C., Quintero M. A. C. and Capozziello S., 2020, *JCAP*, **2020**, 008

⁹<https://healpix.sourceforge.io/>

¹⁰<https://www.tensorflow.org/>

¹¹https://colab.research.google.com/?utm_source=scs-index

- Falk, T., Rangarajan, R. and Srednicki, M., 1992, *Phys. Rev. D*, **46**, 4232
- Fixsen D. J., Cheng E. S., Gales J. M., Mather J. C., Shafer R. A. and Wright E. L., 1996, *ApJ*, **473**, 576
- Gal Y., Hron J., Kendall A., 2017, Concrete Dropout, arxiv.org/abs/1705.07832
- Gangui, A., Lucchin, F., Matarrese, S. and Mollerach, S., 1994, *ApJ*, **430**, 447
- Gómez-Vargas I., Esquivel R. M., García-Salcedo R. and Vázquez J. A., 2021, *Journal of Physics: Conference Series*, **1723**, 012022
- Gómez-Vargas I., Vázquez J. A., Esquivel R. M. and García-Salcedo R., 2021, arxiv.org/abs/2104.00595
- Gorski M. K., Hivon E., Banday J. A., Wandelt D. B., Hansen K. F., Reinecke M. and Bartelmann M., 2005, *ApJ*, **622**, 759
- Graff P., Feroz F., Hobson M. P. and Lasenby A., 2012, *MNRAS*, **421**, 169
- Guth, Alan H. and Pi, So-Young, 1982, *Phys. Rev. Lett.*, **49**, 1110
- Hajian, A. and Souradeep, T., 2004, arxiv.org/pdf/astro-ph/0501001.pdf
- Hanany, S. et al., 2019, arxiv.org/pdf/1902.10541.pdf
- Hansen F. K., Gorski K. M., Hivon E., 2002, *MNRAS*, **336**, 1304
- Hazumi, M. et al., 2020, arxiv.org/pdf/2101.12449.pdf
- Hecht-Nielsen R., 1992, in , *Neural Networks for Perception*. Academic Press, pp 65–93, doi.org/10.1016/B978-0-12-741252-8.50010-8
- Hinshaw G. et al., 2013, *ApJS*, **208**, 19
- Hinton G., Srivastava N., Swersky K., 2012, rmsprop: Divide the gradient by a running average of its recent magnitude, *Neural networks for machine learning—Lecture 6* cs.toronto.edu/hinton/coursera/lecture6/lec6.pdf
- Hivon E., Gorski K. M., Netterfield C. B., Crill B. P., Prunet S. and Hansen F., 2002, *ApJ*, **567**, 2
- Hornik K., 1991, *Neural Networks*, **4**, 251
- Hortua H. J., Volpi R., Marinelli D. and Malago L., 2020, arxiv.org/abs/2011.14276

- Hou Z. et al., 2014, *ApJ*, 782, 74
- Kendall A., Gal Y., 2017, What Uncertainties Do We Need in Bayesian Deep Learning for Computer Vision? [arxiv.org/abs/1703.04977.pdf](https://arxiv.org/abs/1703.04977)
- Kingma D. P., Ba J., 2014, Adam: A method for stochastic optimization arxiv.org/abs/1412.6980
- Lai Y., Shi Y., Han Y., Shao Y., Qi M. and Li B., 2021, arxiv.org/abs/2104.12953
- Maldacena, J., 2003, *Journal of High Energy Physics*, 2003,013
- Mancini A. S., Piras D., Alsing J., Joachimi B. and Hobson M. P., 2022, *MNRAS*, 1365-2966
- Mather J. C., Fixsen D. J., Shafer R. A., Mosier C. and Wilkinson D. T., 1999, *ApJ*, 512, 511
- Moss A., 2020, *MNRAS*, 496, 328
- Olvera J. de D. R., Gómez-Vargas I. and Vázquez J. A., 2021, arxiv.org/abs/2112.12645
- Peebles, P. J. E., 1973, *ApJ*, 185, 413
- Penzias, A. A. and Wilson, R. W. 1965, *ApJ*, 142, 419
- Petroff M. A., Addison G. E., Bennett C. L., Weiland J. L., 2020, *ApJ*, 903, 104
- Pinkus A., 1999, *Acta Numerica*, 8, 143
- Planck Collaboration IV, 2020, *A & A*, 641, A4
- Planck Collaboration VI, 2020, *A & A*, 641, A6
- Reinecke M., Seljebotn D. S., 2013, *A & A*, 554, A112
- Ruder S., 2016, An overview of gradient descent optimization algorithms, arxiv.org/abs/1609.04747
- Sievers J. L. et al., 2013, *JCAP*, 2013, 060
- Stacey J. G. et al., 2018, *International Society for Optics and Photonics*, 10700, 482
- Sudevan V., Saha R., 2020, *ApJ*, 497, 30

- Sun S., Cao Z., Zhu H., Zhao J., 2020, [IEEE Transactions on Cybernetics](#), 50, 3668
- Wandelt, B. D., Hivon, E. and Górski, K. M., 2001, [Phys. Rev. D](#), 64, 083003
- Wandelt B. D. and Hansen F. K., 2003, [Phys. Rev. D](#), 67, 023001
- Wang G. J., Ma X. J., Li S. Y. and Xia J. Q., 2020, [ApJS](#), 246, 13